CEAS Space Journal (2023) 15:761–775
https://doi.org/10.1007/s12567-022-00479-4

ORIGINAL PAPER

Evaluation of aerial vehicle configurations for high-range Mars missions

Victor Zappek[1] · Markus Rinker[1] · Lukas Daxer[1] · Manfred Hajek[1]

Received: 24 February 2022 / Revised: 23 September 2022 / Accepted: 15 November 2022 / Published online: 3 January 2023

Abstract

As part of an envisioned autonomous swarm exploration mission in Valles Marineris on Mars a design investigation of a high-range scout UAV is performed in this work. Two VTOL configurations, a coaxial helicopter and a transition tailsitter, are examined to assess their suitability. A preliminary design framework using Python and the optimization framework OpenMDAO is created using the preliminary design software NDARC. To model the rotor performance, comprehensive analysis simulations are executed using CAMRAD II. Structural 2D-FEM beam models are created for the rotor blades and the wing for weight modeling. Design sizings are executed for operation in the extremely thin atmosphere and the mission performance for a scouting mission as part of the robotic Valles Marineris Explorer (VaMEx) swarm is examined. A behavioral model is created to evaluate the controllability of the configurations. The results for a mission with a cruise flight of 30 km and 1.4 kg of payload show that for such a mission the transition configuration does not offer advantages over a more conventional coaxial helicopter design. To understand design sensitivities and to evaluate the respective effects on vehicle performance parameter sweeps are conducted.

Keywords VaMEx · Mars · Rotorcraft · Preliminary design · Tailsitter · UAV · Valles Marineris · Swarm · Exploration · Performance

Abbreviations

DGW	Design gross weight
HC	Helicopter configuration (coaxial)
MH	NASA Mars Helicopter Ingenuity
TS	Tailsitter configuration
UAV	Unmanned aerial vehicle
VaMEx	Valles Marineris Explorer

List of Symbols

A	Rotor/wing area [m^2]
AR	Aspect ratio
b	Wing span [m]
c	Chord length [m]
c_d	Section drag coefficient
C_D	Drag coefficient
C_L	Lift coefficient
C_P	Power coefficient
C_T	Thrust coefficient
DL	Disk loading [N/m^2]
e_{bat}	Specific energy density [Wh/kg]
e_{drag}	Oswald wing efficiency
f	Component weight fraction
h	Flight altitude [m]
K	Weight model factor
κ	Non-ideal inflow factor
μ_x	Edgewise advance ratio
μ_z	Axial advance ratio
N	Number of rotors/blades
n_z	Load factor
P	Power [W]
r	Radial station [m]
R	Rotor radius [m]
σ	Rotor solidity
V	Flight speed [m/s]
W	Structural mass [kg]
χ	Weight model technology factor
X	Weight model exponent

Subscripts

0	Angle of attack for $C_L = 0$
br	Best range (speed)
cont	Contingency (weight)
des	Design point

✉ Victor Zappek
victor.zappek@tum.de

[1] Institute of Helicopter Technology, Technical University of Munich, Boltzmannstr. 15, 85748 Garching, Germany

eff	Effective (cruise efficiency)
min	Minimum
ref	Reference
tip	Rotor blade tip

1 Introduction

The project *Mars High Range Scout* is part of the VaMEx initiative by the German Space Agency at DLR. The initiative encapsulates multiple projects, research institutes and companies with the aim of developing a diverse robotic swarm for the exploration of the canyon system Valles Marineris on Mars shown in Fig. 1. The swarm will consist of wheeled rovers and crawler robots that will closely examine the surface and take samples. The UAV (unmanned aerial vehicle) maps the environment to identify points of interest for the rovers and crawlers to investigate. The scientific goal of this swarm is to search for potential liquid surface water. In this regard Valles Marineris is an especially promising site on Mars as it lies up to 7 km below the Mars surface and the resulting atmospheric pressure of 13 mbar is above the triple point of water [1]. Additionally, rotorcraft have been defined as a key technology for 'in-situ mobility' on other planets by the Planetary Science and Astrobiology Decadal Survey as they provide access to hazardous terrain [2].

This work shows preliminary design investigations for a scout UAV as part of the VaMEx swarm. Aerial exploration of Mars has been a point of research for decades. Early designs such as the NASA *High-flying Mini-Sniffer* [4] and *Canyon-Flyer* (20 kg) [5] looked at airplane designs that would perform a single exploration mission after deploying mid-air from the entry capsule. The Mini-Sniffer and more recent concepts such as the NASA *ARES* (127 kg) [6] and a Japanese mars airplane (3.5 kg) [7] have been tested in Earth upper atmosphere but none have been deployed on Mars. For repeated near-surface exploration, as required for the VaMEx mission, rotorcraft have become a focus of research since landing on the rough Martian terrain requires vertical take-off and landing (VTOL) capabilities. First studies were conducted in the early 2000s [8] with development at NASA continuing until in 2021 the Mars Helicopter (MH) *Ingenuity* (1.8 kg) [9] completed the first successful powered flight on Mars [10]. Further investigations into Mars rotorcraft, manned and unmanned, show the potential rotorcraft can bring to Mars exploration while also highlighting the significant challenges posed by space travel and the Martian atmosphere [11, 12].

These works also discuss the merit of transition configurations such as tailsitter and tiltwing aircraft for long range Martian exploration due to the improved efficiency of wing-borne cruise flight. The main goal of the presented work is to evaluate the suitability of a transition configuration as a scout UAV for the VaMEx swarm mission. The chosen transition configuration depicted in Fig. 2 is a tailsitter VTOL aircraft. For propulsion the tailsitter is modeled with a coaxial contra rotating 2×2 rotor, consisting of 2 rotor planes with 2 rotor blades each. This design was chosen because it allows a larger rotor disk area to be stowed more compactly than for example a side-by-side configuration. Additionally, there is a significant amount of data available on coaxial rotors in Martian atmosphere due to the recent NASA development of the MH. Furthermore the tailsitter has a 15° swept wing with vertical stabilizers at each end which integrate the landing gear. The trailing edge flaps are flaperons and act as a combined horizontal stabilizer and aileron. Tailsitters have the risk of tipping over when sitting on the ground due to surface winds. The flying wing design reduces this risk since it lowers the center of gravity while in upright configuration compared to a design relying on an empennage. However, no detailed analysis of tipping is conducted since reliable surface wind data is not available for Valles Marineris. Motors, battery and all other core components are housed in an aerodynamic fuselage in line with the rotor mast. The tailsitter takes off vertically, climbs above the cruise altitude and transitions into level flight through a dive maneuver to gain the necessary speed for wing-borne cruise flight.

To assess the performance of this configuration a more conventional coaxial helicopter was chosen for comparison. The helicopter has a similar 2×2 rotor setup to the tailsitter. It does not have an empennage. Fuselage and landing gear are modeled similar to that of the MH [9] shown in Fig. 3.

Fig. 1 Picture of Valles Marineris, from [3]

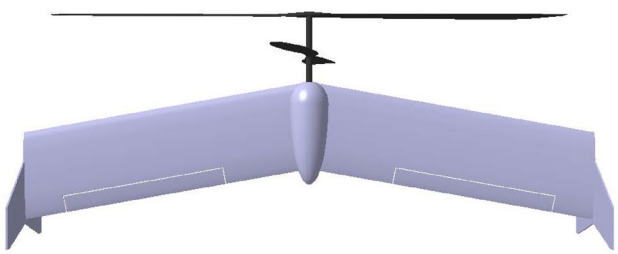

Fig. 2 Tailsitter configuration with coaxial rotor setup

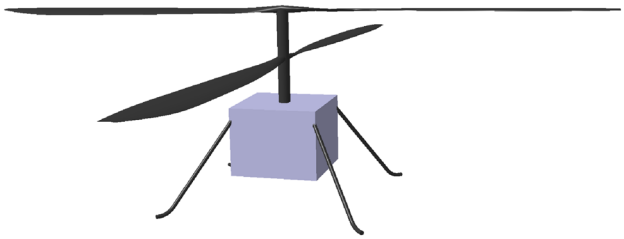

Fig. 3 Coaxial helicopter configuration

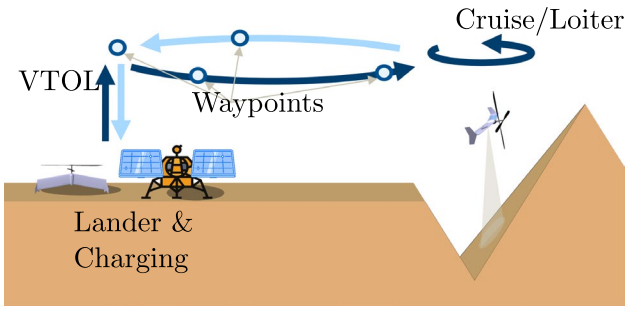

Fig. 4 Visualization of UAV mission profile for exploration of Valles Marineris

The UAV is supposed to return to the lander for charging so that neither configuration integrates a solar cell.

2 Mission requirements

The UAV is part of the VaMEx robotic swarm. This section describes the mission profile of the UAV within the swarm and the atmospheric conditions that the aircraft must operate in.

2.1 UAV mission profile

The planned mission of the VaMEx swarm is the exploration of a region of interest within Valles Marineris. It is planned that the lander also functions as a base station for communications and charging. The ground exploration participants, such as rovers and crawlers, will then investigate points of interest within the region. The task of the UAVs is to map the area and gather image data for swarm-navigation and the identification of these points to optimize the usage of the slower rovers and crawlers [1]. To fulfill this task the gathered scientific data needs to be processed as quickly as possible so that new flights and the movement of the swarm can be planned efficiently. Since mapping will accumulate a significant amount of data and on-board processing needs to be as minimal as possible to reduce processor weight and power, the UAV returns to the lander for charging and download of the accumulated science data. Heavy solar panels for recharging are thereby also made redundant and enabling consistent operation even in Martian winter when solar cells wold not provide sufficient energy. Mapping and data acquisition are planned to be executed during cruise flight. Therefore, the mission does not require a prolonged hover segment. Instead, it consists only of take-off, climb, cruise, descent and landing, as shown in Fig. 4. For the transition configuration the climb segment also includes a climb above cruise altitude to represent the transition maneuver.

The VaMEx requirements, derived from earlier investigations in predecessor projects, define a return mission with an operations radius of 14 km, so a total of 28 km, as the minimum range. A maximum achievable range is to be identified in the study, with 100 km as an ideal target for a more complex mission that incorporates multiple points of interest. As initial design point a total flight distance of 30 km is set. This represents the required operations radius including slight deviations from a direct course.

The required payload capacity, comprising of science sensors, cameras and other electronic components, is estimated from similar terrestrial configurations as 1.4 kg.

The main mission parameters are shown in Table 1. The total hover time represents the time spent in hover for take-off and landing. The tailsitter is assumed to fly faster in cruise since parasitic drag of the configuration is lower and because the necessary wing area inversely correlates to the cruise speed leading to smaller and lighter wings at higher speeds. These cruise speeds are a baseline and can be adapted should the results show a need to do so. Payload and range growth potential apart from the initial design point are investigated in Sect. 4.2.

2.2 Atmospheric conditions

The atmosphere of Mars in general poses several challenges for any kind of vehicle. The thin atmosphere leads to high variations in temperature of up to ±120 K and strong solar radiation on the surface. The composition of the atmosphere, which consists mainly of over 95 % CO_2 [13] means that no oxidizing power sources can be used. For aircraft the atmospheric density ρ and the gravitational acceleration g are the most relevant factors in regards to lift generation. The mean surface air density on Mars is only $\rho_{\text{mean, surface}} = 0.02\ \text{kg/m}^3$

Table 1 Summary of mission parameters for Mars UAV scout mission

Payload	1.4 kg
Total hover time	40 s
Total flight distance	30 km
Cruise altitude	200 m
Cruise speed (HC)	40 $\frac{\text{m}}{\text{s}}$
Cruise speed (TS)	80 $\frac{\text{m}}{\text{s}}$

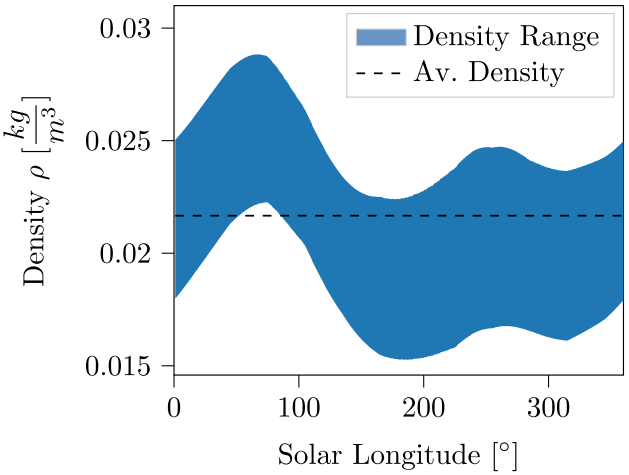

Fig. 5 Density range and average density in Valles Marineris (13.995° *S*, 58.332°*W*, 5 m above surface), from [16]

Table 2 Average atmospheric conditions on Earth, Mars Surface and Valles Marineris (VM), from [13] [16]

	Earth	Mars	VM
Grav. acc g [$\frac{m}{s^2}$]	9.81	3.71	3.71
Temperature T [K]	288	210	218
Pressure p [Pa]	101325	636	895
Density ρ [$\frac{kg}{m^3}$]	1.225	0.02	0.022
Dyn. visc. η [$\frac{kg}{ms}$] $\times 10^{-5}$	1.7	1.1	1.1
Speed of sound a [$\frac{m}{s}$]	340	233	235

which is less than 2 % of the mean terrestrial air density. Meanwhile g is 3.71 m/s^2 or approximately 38 % of Earth gravity [13]. This makes generating the required lift for powered flight challenging and necessitates extremely lightweight construction. The lower air density also leads to lower Reynolds numbers *Re* than on Earth which affects aerodynamic airfoil performance, especially regarding the minimum drag coefficient $C_{D,min}$. These Reynolds effects are discussed in more detail in Sect. 3.3.

To narrow down the mission environment for the design of the rotorcraft, a reference point is defined in the canyon. Following [14] and [15] a low point in Valles Marineris at $h = -5210$ m is identified at 13.995°S, 58.332°W. Because of the depth of Valles Marineris its atmospheric conditions differ from the average Martian conditions. The lower altitude leads to a higher average temperature and density. Fig. 5 shows the yearly density variation in Valles Marineris and the yearly average. Since precise mission planning has not been conducted yet, so that the exact flight times are unknown, the yearly average is used for these investigations. The average values for all relevant atmospheric parameters are shown in Table 2. Since this data is derived from models and the exact operation time and Martian season is not final the influence of varying air densities on the design is investigated in Fig. 15.

Another aspect that makes VTOL operation on Mars more difficult than on Earth is the lower speed of sound which restricts the maximum rotational speed of the rotor. Further atmospheric characteristics such as winds, dust and high radiation are not considered in these early investigations but have to be taken into account for detailed designs.

3 Sizing methodology

To evaluate the performance of both configurations for the given mission parametric models have to be created that can be used to perform design sizings. In this section, the software environment used to create the underlying models and to perform these investigations are presented.

3.1 Software environment

For the design sizings and performance evaluations at the core of these investigations the NASA preliminary design software *NASA Design and Analysis of Rotorcraft* (NDARC) [17] is used. Through the Python interface RCOtools [18] NDARC is connected with the optimization framework OpenMDAO through which Design of Experiment investigations can be automated [19]. The comprehensive analysis tool CAMRAD II is used for rotor power analysis and the structural rotor blade design environment SONATA is employed for weight modeling of rotor blades and tailsitter wing. Figure 6 shows the tools used and how they are connected.

3.2 NDARC

NDARC is a program for preliminary design, sizing and performance analysis of new aircraft with a focus on VTOL configurations. The sizing algorithm designs the aircraft to satisfy a set of constraints and missions. Analysis tasks include out-of-design mission analysis and flight performance calculations for specific points in the flight envelope. Aircraft size is characterized by parameters such as total aircraft weight, empty weight, component dimensions, battery capacity, and engine or motor power. To achieve flexibility in configuration modeling, NDARC designs an aircraft from a set of components, including fuselage, wings, empennage, rotors, gearboxes, and engines. For efficient program execution, each component is represented by a surrogate model for performance and weight estimation. Component models can be calibrated with higher fidelity modeling software as well as databases of existing components. The reliability of

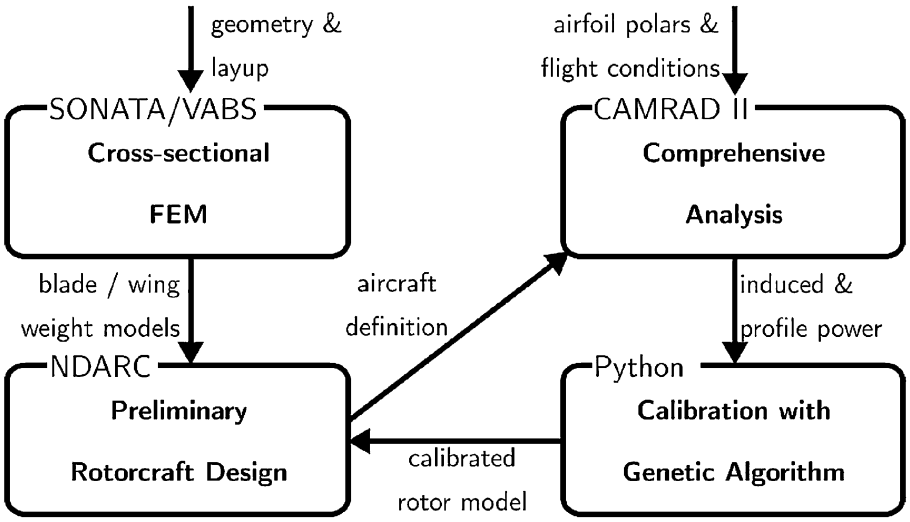

Fig. 6 Preliminary design software environment

the computational results depends on the accuracy of the calibrated component models.

NDARC's rotor performance model is based on an extended momentum theory.

$$P_{req} = P_{comp} + P_{xmsx} + P_{acc} \tag{1}$$

$$P_{comp} = P_i + P_0 + P_p + P_t \tag{2}$$

$$P_i = \kappa P_{i,ideal} \tag{3}$$

$$\kappa = f\left(\frac{C_T}{\sigma}, \mu, \ldots\right) \tag{4}$$

$$P_0 = \rho A V_{tip}^3 C_{P0} \tag{5}$$

$$C_{P,0} = \frac{\sigma}{8} c_{d,mean} F_p \tag{6}$$

$$c_{d,mean} = f\left(\frac{C_T}{\sigma}, \mu, \ldots\right). \tag{7}$$

The required power P_{req} is described as the sum of component power P_{comp}, transmission losses P_{xmsx}, and auxiliary power losses P_{acc} (1). The component power (2), is thereby the sum of the induced, profile, parasitic, and interference power terms [20]. The terms for induced (3) and profile power (5) are extended by surrogate models to represent rotor characteristics that go beyond classical momentum theory. The induced power model accounts for non-uniform inflow and blade tip losses through the correction factor κ as a function of the advance ratio μ and the blade loading C_T/σ. Similarly, the profile power (5) is calculated with a non-constant mean section drag coefficient $c_{d,mean}$ (7) including surrogate models for flow detachment, Mach, and Reynolds number effects [21]. F_P considers effects of varying relative flow conditions at the blade elements.

3.3 Rotor model calibration using CAMRAD II

To improve modeling accuracy the parameters of the aforementioned rotor surrogate models for κ and $c_{d,mean}$ should be calibrated [17] especially in this context since Martian rotorcraft aerodynamics differ considerably from terrestrial applications. For this purpose the comprehensive analysis tool CAMRAD II is used to model the rotor aerodynamics. CAMRAD II uses blade element theory for rotor power calculations and it can model blade dynamics and blade deformations. Since these studies focus on rotor power the rotor dynamics are neglected and the rotor blades are modeled as rigid. The NDARC rotor model calibration includes the following steps:

- Generation of CAMRAD II model from airfoil polars and rotor geometry
- Validation with hover results from MH data
- Derivation of scaled models for investigated configurations
- CAMRAD II sweeps (C_T/σ, μ_x or μ_z)
- Calibration of NDARC rotor model using genetic algorithm

A baseline CAMRAD II model using uniform inflow modeling is built based on the blade geometry [22] and airfoil data of the MH. This baseline model is then validated using data from a MH hover flight test, shown in Fig. 7. CAMRAD II models for the helicopter and tailsitter configuration are derived with the main difference being a higher blade twist

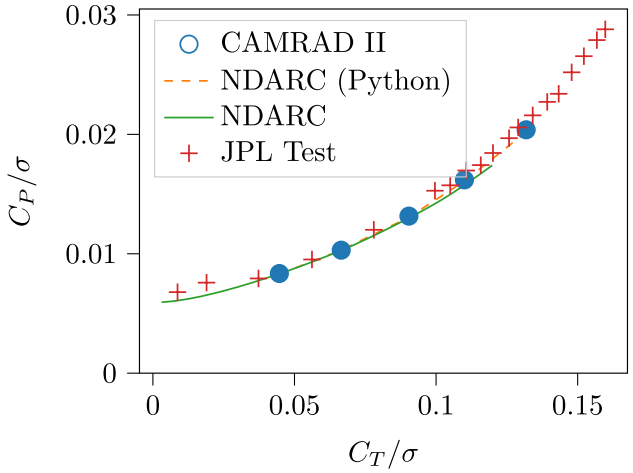

Fig. 7 Validation of NDARC rotor model calibration with MH data from [23]

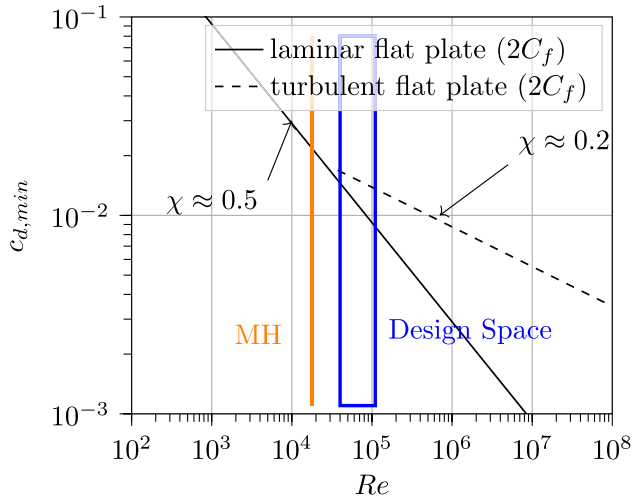

Fig. 8 Minimum section drag coefficient $c_{d,min}$ versus Reynolds number Re, derived from [24]

for the tailsitter rotor to account for the cruise flight in which the rotor operates as a propeller. The modeled rotors have a radius of $R = 1.2$ m compared to the MH with a radius of $R_{MH} = 0.605$ m since early investigations showed the need for a much larger rotor. Two flight state sweeps, one covering hover operation and one cruise flight, are taken into consideration for each configuration. For the hover sweep C_T/σ is varied. For helicopter cruise flight C_T/σ and the forward advance ratio μ_x are varied, whereas for the tailsitter the axial advance ratio μ_z is used to represent propeller operation. Because propeller operation is modeled the values for C_T/σ are also lower than for the helicopter since the rotor thrust only counteracts drag and does not provide lift.

To derive NDARC rotor models from these parameter sweeps a calibration tool is created. For this the NDARC models were implemented in Python in isolation to speed up and simplify model calibration. For minimization of the error between CAMRAD II values and corresponding NDARC rotor model calculations OpenMDAO is used. OpenMDAO provides numerous optimization algorithms. Because the NDARC rotor models include Boolean and absolute statements gradient-based optimization algorithm might run into local minima. For this reason a genetic algorithm is employed [19]. Fig. 7 shows a verification of calibration results of the implemented performance functions compared to NDARC calculations.

The larger rotor blades investigated here lead to higher Reynolds numbers compared to the MH from which the airfoil data is taken. This influences airfoil performance and especially the drag characteristics. To take this effect into account Reynolds scaling is applied to the calibrated NDARC model for $c_{d,mean}$ in form of Eq. (8) [21].

$$c_{d,mean,scaled} = \left(\frac{Re_{ref}}{Re(r = 0.75R)} \right)^{\chi} c_{d,mean} \tag{8}$$

The exponent χ depends on the flow regime that the airfoils operate in. Fig. 8 shows the relation between the minimum drag coefficient $c_{d,min}$ of flat plates with laminar and turbulent flow and the operating Reynolds number. For laminar flow the increase of $c_{d,min}$ at lower Re is more pronounced at an exponent of $\chi \approx 0.5$ compared to 0.2 for the turbulent flat plate. Since the expected Reynolds number range lies between 50000 and 100000 which is in between the two regimes a conservative estimate of $\chi = 0.3$ is used.

3.4 Weight model calibration using SONATA

During early design investigations it became apparent that the structural weight of the rotor blades is especially critical for the resulting design gross weight (DGW) of the sized rotorcraft [25]. For this reason the multidisciplinary rotor blade design environment SONATA is employed to model the rotor blades [26]. The integrated structural mesher SONATA-CBM generates the three-dimensional structure of the blade or similar slender bodies from the definition of the cross-sectional material lay-up at different radial/lengthwise stations and from the distribution of sweep, twist and chord at these stations. SONATA is coupled with the analysis tool VABS which splits the three-dimensional elastic problem into a two-dimensional linear cross-section analysis and a one-dimensional nonlinear beam analysis [27]. VABS is used to calculate blade properties including the weight. To improve weight prediction of the tailsitter wing a SONATA model of the wing is created as well.

Geometry and lay-up of the rotor blades are based on the MHS010 blades of the MH [22]. The layup at the radial

station $r/R = 0.3$ as modeled and meshed in SONATA-CBM is shown in Fig. 9. The bidirectional skin fibers of the MHS010 are modeled as a +45° and a −45° unidirectional layer. The inner spar consists of multiple layers of unidirectional 0° fibers. The middle section of the blade is reinforced with additional spar layers that do not wrap around leading and trailing edge. ROHACELL 32 IG-F is used as foam-core filler.

The blade model does not include any detailed blade root inserts for connection of the blade to the rotor hub. Also, Chinese weights [9] for reduction of actuator torque requirement, as well as pitch horns were neglected. However, there is no information available whether these weights were included in the original MHS010 blade weight or whether they belong to the flight controls weight. Therefore, these simplifications may lead to a more optimistic blade weight. Meshing issues for very thin airfoils limited minimum ply thickness and lead to a slightly higher blade weight. This aspect may partially compensate for the neglected blade root inserts and dynamic tuning weights. Published MHS010 blade weights range from 33 g [9] to 43 g [28]. The final MHS010 rotor blade modeled in SONATA has a weight of 39.5 g, which is found to be sufficiently accurate. Additionally, the modeled structure is evaluated using VABS. The maximum expected lift force and centrifugal force are applied and the minimum safety factor is found to be above 3. No dynamic loads are examined.

From this baseline model geometrically scaled versions are derived with SONATA by varying the radius and chord. From these the parameters of a customized NDARC blade weight model (9) are calibrated. The model calculates the rotor blade weight (per blade) from a constant factor K_{blade} and the exponents $X_{blade,R}$ and $X_{blade,c}$ which influence how the blade weight scales with the radius R and the chord length c. The calibrated parameter values are shown in Table 3.

$$W_{blade} = K_{blade} R^{X_{blade,R}} c^{X_{blade,c}}. \tag{9}$$

Figure 10 shows the cross-section of the tailsitter wing modeled in SONATA. The airfoil used for this wing is the Ishii airfoil, which has been designed for a Japanese Mars airplane [29]. The skin is modeled as a composite sandwich

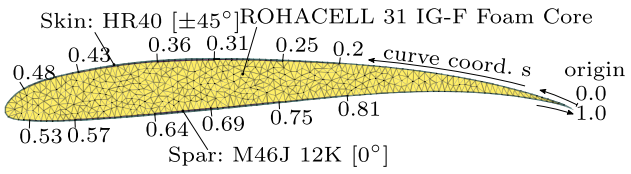

Fig. 9 Cross section of the MHS010 blade modeled in SONATA at $r/R = 0.3$

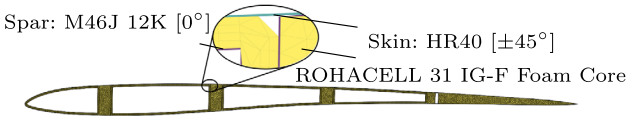

Fig. 10 Cross section of tailsitter wing modeled in SONATA

structure with a +45° and a −45° unidirectional layer as the outer skin and two unidirectional 0° layers on the inside of the foam filler. The three bridges and the endcap before the trailing edge consist of a foam core with two unidirectional layers on the outside. To more accurately predict the weight of the assembled wing including the flaperons, the trailing edge is modeled in the same way as the bridges.

The standard NDARC wing weight model for non-folding wings (AFDD93) [21] (10) models the weight depending on the DGW, the wing sweep $\Lambda_{wing} = 10°$, the design load factor $n_{z,wing}$, the taper ratio λ_{wing}, the airfoil thickness ratio $\frac{t}{c}_{wing}$ and the projected wing area A_{wing}. Since the model is based on general aviation aircraft, it is calibrated using the technology factor χ_{wing} to match the modeled wing at the design wing loading WL. [Note: Eq. (10) uses imperial units]

Table 3 Summary of important model input parameters for sizing of helicopter (HC) and tailsitter (TS) configuration in NDARC

	HC	TS
$DL\,[\frac{N}{m^2}]$	5.5	5.5
$\frac{C_T}{\sigma}_{des}$	0.1	0.1
$M_{tip,hover}\,[\frac{m}{s}]$	0.8	0.8
$M_{tip,cruise}\,[\frac{m}{s}]$	0.8	0.68
K_{blade}	2.48	2.48
$X_{blade,R}$	0.9775	0.9975
$X_{blade,c}$	1.391	1.391
$C_{D,fuselage}$	0.2	0.03
$C_{L,wing,des}$	–	0.55
$C_{L,wing,stall}$	–	0.9
$C_{D,0,wing}$	–	0.025
$C_{L,Dmin,wing}$	–	0.0
$e_{drag,wing}$	–	0.8
AR_{wing}	–	6
$n_{z,wing}$	–	3
Λ_{wing}	–	10°
λ_{wing}	–	1
t/c_{wing}	–	0.07
χ_{wing}	–	1.3825
$e_{bat}\,[\frac{Wh}{kg}]$	278	278
$f_{w,LG}$	0.067	0.0335
$f_{w,cont}$	20 %	20 %

$$W_{wing} = \chi_{wing} 5.66411 \left(\frac{DGW}{1000 \cos \Lambda_{wing}}\right)^{0.847} n_{z,wing}^{0.39579} A_{wing}^{0.21754} \left(\frac{1+\lambda_{wing}}{t/c_{wing}}\right)^{0.09359}. \quad (10)$$

Since there is no reference structure for the wing, a simplified structural analysis of the expected lifting loads is used. A constant lift distribution with a load factor of $n_z = 3$ is applied and the wing root cross-section is analyzed with VABS. The result is that no point within the cross-section shows a safety factor below two. This is found to be sufficient as a plausibility test for the created wing structure. However, it has to be noted that these structural investigations did not take into account dynamic loads or buckling loads.

3.5 NDARC model parameter inputs

As stated in Sect. 3.2 NDARC aircraft models consist of component models which again can be split up into surrogate models regarding aircraft performance and weight models. The total parameter set is too large to include in this paper but an excerpt of the most important modeling parameters is presented here and the respective values are summarized in Table 3.

The rotor sizing can be based on different parameters depending on operating conditions and boundary conditions such as size constraints from a lander. Since there is no lander geometry available at this time, the disk loading DL, the blade loading C_T/σ and the rotor hover tip Mach number $M_{tip,hover}$ are chosen as design inputs for the sizing of the rotor. DL determines the area of the rotor disk A_{disk} as a constant relation to DGW.

$$DL = \frac{DGW \cdot g}{A_{disk}} \quad (11)$$

$$A_{disk} = \frac{DGW \cdot g}{DL} = N_{rotor} \pi R^2. \quad (12)$$

The chosen disk loading DL represents a compromise between a larger rotor disk which reduces the required induced power in hover and correspondingly increasing rotor blade length with unrealistically slender blades. The design blade loading C_T/σ_{des} is the ratio of design thrust $DGW \cdot g$ to blade area A_{blade} normalized with ρ and the blade tip speed $v_{tip} = M_{tip} \cdot a$. It determines the total blade area of the rotor.

$$\frac{C_T}{\sigma}_{des} = \frac{\frac{DGW \cdot g}{\rho A_{disk} v_{tip}^2}}{\frac{A_{blade}}{A_{disk}}} = \frac{DGW \cdot g}{\rho A_{blade} v_{tip}^2} \quad (13)$$

$$A_{blade} = \frac{DGW \cdot g}{C_T/\sigma \cdot \rho \cdot v_{tip}^2} = N_{rotor} N_{blade} cR \quad (14)$$

The design value is dependent on the airfoil performance and should be chosen so that there is a thrust margin between required hover thrust and the point of blade stall. Since the rotor blades are modeled after those of the MH C_T/σ_{des} is also taken from the MH design [28]. The MH has a thrust margin in hover of $C_{T,stall}/C_{T,des} \approx 1.5$ [23]. The tip Mach number in hover $M_{tip,hover}$ is chosen so that the tip mach number of the advancing blade in helicopter cruise flight does not exceed 0.95. For the tailsitter configuration, the tip speed is modeled to be lower in cruise flight to reduce cruise power in propeller operation [30].

The wing loading WL and the aspect ratio AR determine the wing area A_{wing} and span b_{wing}. At a fixed cruise speed v_{cruise} WL is directly proportional to a design wing lift coefficient $C_{L,wing,des}$.

$$WL = \frac{DGW \cdot g}{A_{wing}} = \rho v_{cruise}^2 C_{L,wing,des} \quad (15)$$

$$A_{wing} = \frac{DGW \cdot g}{C_{L,wing,des} \cdot \rho v_{cruise}^2} = b_{wing}^2/AR. \quad (16)$$

Compared to terrestrial operation the wing airfoil will operate at drastically lower Reynolds numbers. While notable progress in the design and optimization of airfoils for these conditions has been conducted their lift and drag performance in the expected Reynolds numbers range does not match that of conventional airfoils under terrestrial conditions [31–33]. Therefore, $C_{L,wing,des}$ is set lower than for equivalent terrestrial configurations. The value shown in Table 3 is estimated from low Reynolds number airfoil investigations [31–33] and the high-altitude test of a Japanese Mars airplane design [7]. The parameters of the NDARC wing drag model (17) and the maximum wing lift coefficient at which stall occurs $C_{L,wing,stall}$ were also estimated from these references.

$$C_{D,wing} = C_{D,0,wing} + \frac{(C_L - C_{L,0})^2}{AR \cdot \pi \cdot e_{drag,wing}}. \quad (17)$$

Since the helicopter configuration is modeled after the MH the fuselage drag is modeled accordingly [28]. For the tailsitter an aerodynamic fuselage with a lower drag coefficient $C_{D,fuselage}$ is modeled [34] because of the higher cruise speed. The drag coefficients refer to the wetted fuselage area in this case.

Rotor blade weight and wing weight are modeled according to Sect. 3.4. For the stabilizers the same weight model as for the wings is employed. The landing gear weight is modeled as a fraction of aircraft weight $f_{w,LG}$. The value

for the helicopter configuration is based on the MH. For the tailsitter $f_{w,LG}$ represents the structural reinforcement of the stabilizers that the aircraft stands on and is assumed to be 50 % of the value used for the helicopter. Weight models for the fuselage, motors and flight controls are derived from the MH [28]. To ensure control authority the motors are sized so that maximum power is 150% of hover power. For the specific battery energy density e_{bat} an estimation from a JPL technology forecast [35] is used. To account for uncertainties in the modeling an additional contingency weight factor $f_{w,cont}$ is applied to the aircraft weight. This factor is currently set at 20 %, which can be considered moderate to low since uncertainty overall is high at this early design stage. Since most of the baseline data is based on published weight information of the MH 20 % is considered reasonable. Less data is available for tailsitter configurations especially for Martian operation. Higher values for $f_{w,cont}$ might, therefore, be appropriate here. The influence of more conservative contingency margins is examined in Sect. 4.2.

4 Results and discussion

In this section, the resulting sized configurations for the initial design conditions are presented. To discuss dependencies and uncertainties in the modeling, sweeps of mission and design parameters are presented. Additionally, a simplified investigation of the control characteristics is conducted and is presented here.

4.1 Results at design point

Table 4 shows the dimensions and the weight breakdown of the helicopter and tailsitter aircraft as sized by NDARC using the presented model parameters. The avionics weight and payload are fixed values and represent electronic components that do not depend on the aircraft size. The weight breakdown shows that for a mission with a range of 30 km and a payload of 1.4 kg the sized design gross weight of the tailsitter is higher than that of the helicopter. Consequently its rotor radius is larger as well.

When looking at component weights it stands out that the battery weight of the tailsitter is lower than that of the helicopter despite the higher overall aircraft weight. This is due to the superior effective cruise efficiency $(L/D)_{eff}$ of the tailsitter compared to the helicopter. $(L/D)_{eff}$ is calculated as the relation between useful power $DGW \cdot g \cdot V$ and the actual consumed power P(18).

$$\left(\frac{L}{D}\right)_{eff} = \frac{DGW \cdot g \cdot V}{P}. \tag{18}$$

Table 4 Geometry and weight breakdown of helicopter (HC) and tailsitter (TS) configuration sized for a mission with 30 km total range and 1.4 kg payload

	HC	TS	
R_{rotor} [m]	1.52	1.68	
A_{wing} [m^2]	–	2.4	
b_{wing} [m]	–	3.83	
	m [kg]	m [kg]	x_{CG} [m]
Rotor	2.8	3.5	−0.45
Fuselage	1.4	2.5	0.016
Wing	–	3.4	1.3
Stabilizers	–	0.8	0.43
Motors	1.6	2.0	−0.15
Battery	5.4	3.9	0.21
Landing gear	1.4	0.9	0.43
Flight controls	1.9	2.4	−0.45
Avionics*	0.8	0.8	0.0
Payload*	1.4	1.4	0.0
Contingency	3.8	4.8	0.0
DGW	21.5	26.4	−0.051

Additionally, the center of gravity x-position of components and overall aircraft are given for the tailsitter configuration (positive = aft)

*Fixed

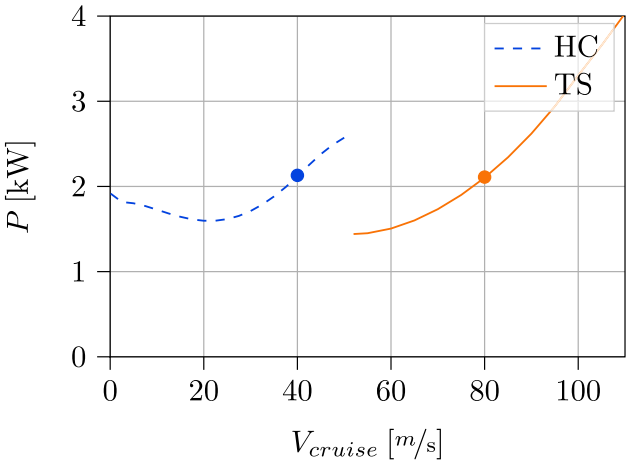

Fig. 11 Comparison of power in cruise flight for resulting coaxial helicopter (HC) and tailsitter (TS) aircraft at design point.

Figure 11 shows that the cruise efficiency of the tailsitter is more than double that of the helicopter since both configurations have a similar power demand in cruise but the tailsitter flies at double the speed. This is due to the wing-borne cruise which in turn reduces the required energy to fly the mission. For the helicopter configuration the design cruise speed $V_{cruise,des}$ is equivalent to the best range speed V_{br} of the configuration. For the sized tailsitter the resulting

V_{br} is 70 m/s. The reason why $v_{cruise,des}$ is kept at 80 m/s is discussed in Sect. 4.2.

While the superior cruise efficiency of the tailsitter leads to lower battery weights, the added weight of wing and stabilizers negate these positive effects and lead to an overall heavier aircraft. No fixed dimensions or requirements for the lander storage geometry are available yet but it is likely that the wing span b_{wing} of almost 4 m would necessitate a complex folding mechanism or a large storage space in the lander. Detailed studies in this regard must be conducted once a lander geometry is found.

4.2 Parameter sensitivities

Sweeps of mission and design parameters were conducted to discuss the influence of deviations from the expected parameter values on the sized DGW. Figure 12 shows the dependency between the sized aircraft design gross weight DGW and the mission range. At the minimum required range for the VaMEx mission of 30 km and lower, the tailsitter is heavier than the helicopter. For higher ranges the margin decreases. Further examinations show that above a range of 40 km the sizing actually leads to a lower DGW for the tailsitter. This shows that a tailsitter configuration does have merits for high range applications. However, tailsitter aircraft designed for these higher ranges are significantly larger and heavier than those designed for the initial range. For ranges above 45 km no converged solution is found for either configuration due to the ever faster increasing DGW that leads to the sizing loop diverging.

For the payload a mostly linear correlation for both configurations can be seen in Fig. 13. Therefore, by adjusting the payload requirements the aircraft size could be influenced

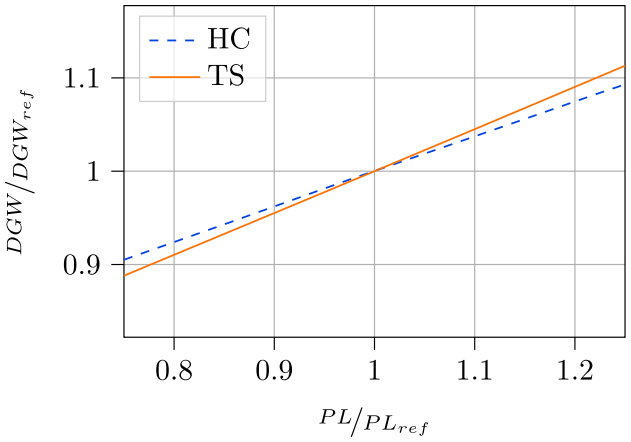

Fig. 13 Dependence of sized DGW from payload for coaxial helicopter (HC) and tailsitter (TS). DGW_{ref} = 21.5 kg (HC) 26.4 kg (TS) PL_{ref} = 1.4 kg (HC) 1.4 kg (TS)

or alternatively payload capacity could be traded for battery capacity and thereby range.

For both configurations, the cruise speed v_{cruise} is set constant in the sizing loop to improve numerical stability of the inner iterations of the NDARC calculations. Since the best range calculation is not conducted during sizing, the influence of various values of v_{cruise} on the sized DGW is investigated and the results can be seen in Fig. 14. For the helicopter configuration a minimum in DGW can be seen at the design cruise speed v_{cruise} = 40 m/s since this coincides with V_{br} as also shown in 11. Higher speeds lead to increasing trimmed pitch angles in cruise due to the lack of horizontal stabilizers which limits the maximum speed.

The tailsitter shows a significant connection between DGW and v_{cruise}. Despite the lower best range speed shown

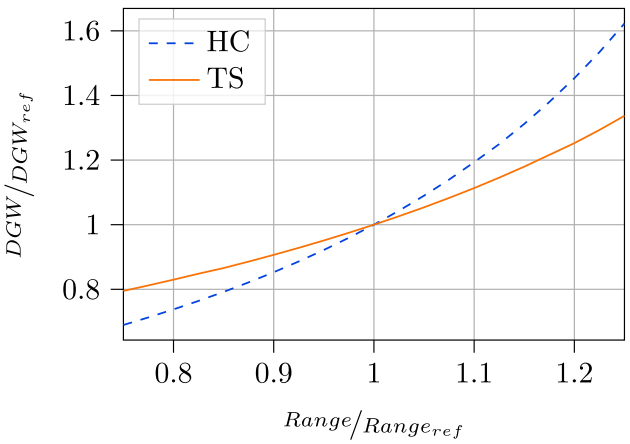

Fig. 12 Dependence of sized DGW from mission range for coaxial helicopter (HC) and tailsitter (TS). DGW_{ref} = 21.5 kg (HC) 26.4 kg (TS) $Range_{ref}$ = 30 km (HC) 30 km (TS)

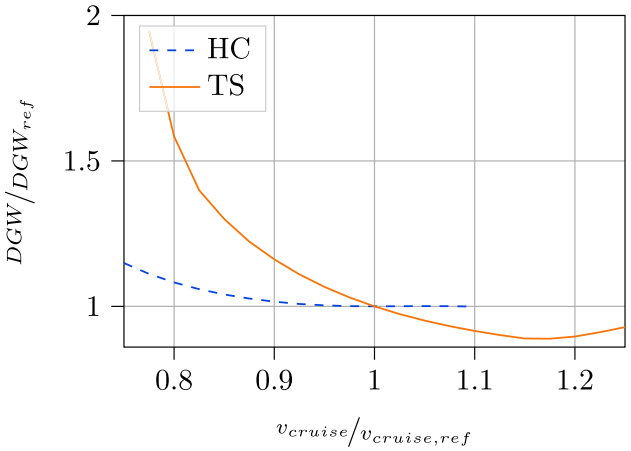

Fig. 14 Dependence of sized DGW from cruise speed for coaxial helicopter (HC) and tailsitter (TS). DGW_{ref} = 21.5 kg (HC) 26.4 kg (TS) $v_{cruise,ref}$ = 40 m/s (HC) 80 m/s (TS)

in Fig. 11, lower speeds lead to a sharp increase in sized weight, while slightly higher speeds could lead to lighter configurations than the one shown in Table 4. The main factor contributing to this trend is that for this examination the wing lift coefficient $C_{L,wing,des}$ during cruise is kept constant. Therefore, the wing size and weight increase for slower cruise speeds. For faster cruise an optimum between wing size and drag can be found around $v_{cruise} = 90$ m/s. Nevertheless, the cruise speed is kept at 80 m/s because initial investigations of possible camera hardware found that the exposure time at higher speeds becomes too low.

As mentioned in Sect. 2.1 the exact operation area within Valles Marineris and also the exact time that the flights will be carried out at have not yet been defined. Hence, the atmospheric density ρ could change in the final design. Fig. 15 illustrates that the tailsitter sizing is extremely dependent on the density ρ while the helicopter shows a lower but still significant correlation. At lower densities the rotor blade (14) and wing area (16) increase, since C_T/σ_{des} and $C_{L,wing,des}$ are kept constant. Because the tailsitter is affected at both rotor and wing, its design is extremely dependent on ρ.

However, if flights could, for example, be limited to Martian winter, the design density could be increased which would lead to more beneficial results for the tailsitter configuration.

The aerodynamic airfoil performance of the rotor blades and the wing is a key difference to terrestrial operation. The values set for the design blade loading C_T/σ_{des} and the design wing lift coefficient $C_{L,wing,des}$ were chosen conservatively based on MH data for the blades and low Reynolds number airfoil investigations for the wing [7, 31–33]. Fig. 16 shows how the sized weight changes with higher blade loadings that imply improved airfoil performance. Increased blade loading leads to a smaller required blade area and a lower DGW with the trend being similar for both configurations. For this design parameter, a conservative stall margin needs to be maintained for maneuverability. Hence, the design point cannot be chosen at the absolute performance optimum. The design value selected here is based on the MH. Currently NASA is actively working on improving Martian rotorcraft performance within the *ROAMX* project [36]. A key factor in this are thin airfoils that can provide better performance at low Reynolds numbers. The studies show a possible increase in design blade loading of at least 10% [37]. However, these thin airfoils introduce structural challenges regarding the necessary stiffness to achieve the required control bandwidth which is why further investigations would be needed to consider them in such a design [28].

A similar dependency can be seen for the tailsitter wing in Fig. 17. The weight is very sensitive to changes in the design lift coefficient. An increase of 25 % to $C_{L,\,\mathrm{wing,\,des}} = 0.69$ results in a 15 % decrease in DGW. The main driving factor

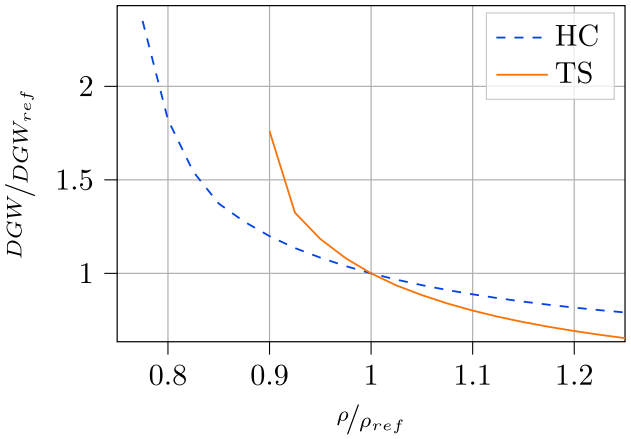

Fig. 15 Dependence of sized DGW from design air density for coaxial helicopter (HC) and tailsitter (TS). $DGW_{ref} = 21.5$ kg (HC) 26.4 kg (TS) $\rho_{ref} = 0.022\,\mathrm{kg/m^3}$ (HC) $0.022\,\mathrm{kg/m^3}$ (TS)

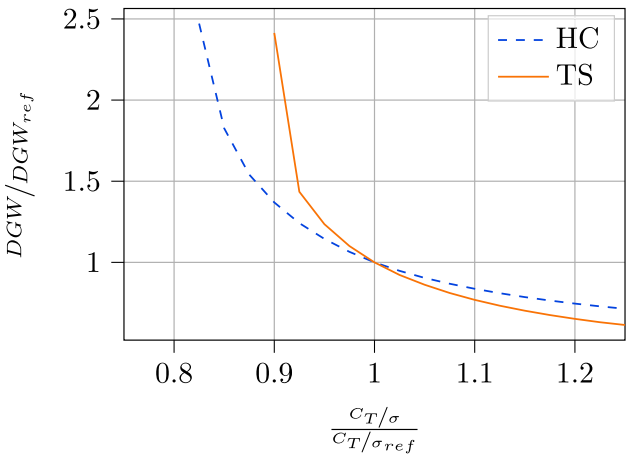

Fig. 16 Dependence of sized DGW from design blade loading for coaxial helicopter (HC) and tailsitter (TS). $DGW_{ref} = 21.5$ kg (HC) 26.4 kg (TS) $C_T/\sigma_{ref} = 0.1$ (HC) 0.1 (TS)

in the weight dependency from blade loading and wing lift coefficient is the structural weight of blades and wings, since higher airfoil performance reduces the required lift surface as described in Eqs. (14) and (16).

To evaluate whether higher design values of C_T/σ and $C_{L,\,\mathrm{wing}}$ might be feasible, additional aerodynamic simulations and tests would have to be conducted.

The disk loading *DL* determines the size of the rotor disk. In principle a larger rotor reduces the induced velocity which reduces induced power. *DL* also determines the rotor solidity σ (at constant v_{tip} and $C_T/\sigma_{\mathrm{des}}$) and thereby the blade chord c. Combined with the blade weight model (9), which has a higher exponent for chord variation than for the radius, this leads to a high sensitivity of DGW from *DL* depicted in Fig. 18. When looking only at this data it seems logical to

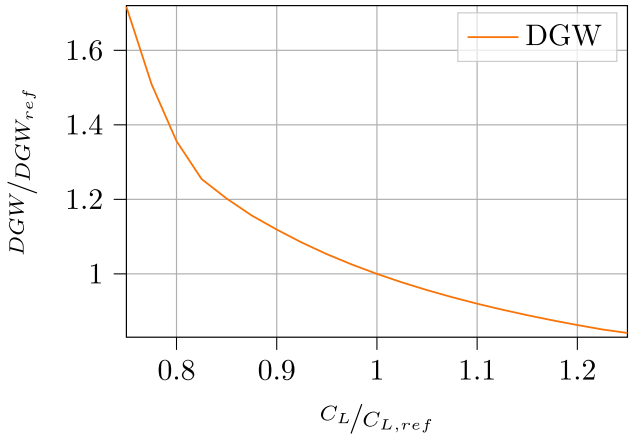

Fig. 17 Dependence of sized DGW from Wing lift coefficient for tailsitter (TS). $DGW_{ref} = 26.4\,\text{kg}$ $C_{L,wing,ref} = 0.022\,\text{kg/m}^3$

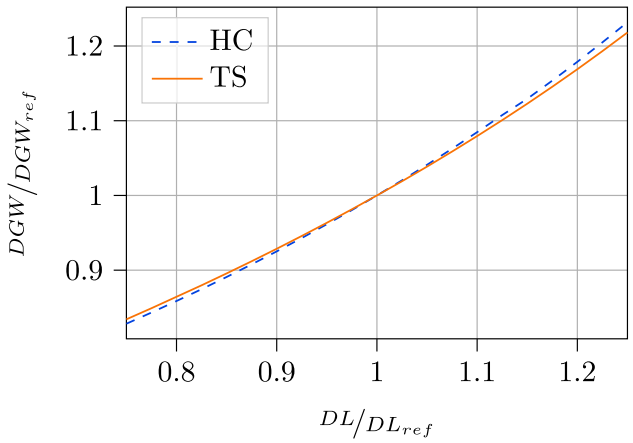

Fig. 18 Dependence of sized DGW from design disk loading for coaxial helicopter (HC) and tailsitter (TS). $DGW_{\text{ref}} = 21.5\,\text{kg}$ (HC) $26.4\,\text{kg}$ (TS) $DL_{\text{ref}} = 5.5\,\text{N/m}^2$ (HC) $5.5\,\text{N/m}^2$ (TS)

set DL much lower. However, since this would lead to very slender rotor blades the feasibility of such blades should be studied first. In [28], structural rotor blade designs for future NASA mars missions are investigated and it is found out that larger and more slender blades require structural reinforcement to meet flap eigenfrequency requirements. Therefore, it is decided to keep the initial disk loading of $DL = 5.5\,\text{N/m}^2$ which results in a similar blade geometry to the MH that the model was derived from. At this disk loading Fig. 18 also shows a minimum of the rotor radius R which is beneficial. In detailed designs at a later point, the rotor size will likely be constricted by the lander geometry that has yet to be determined.

The influence of differing weight models for the rotor blades and the wing are examined by applying a technology factor K_{tech} to the respective weight model. Fig. 19 shows

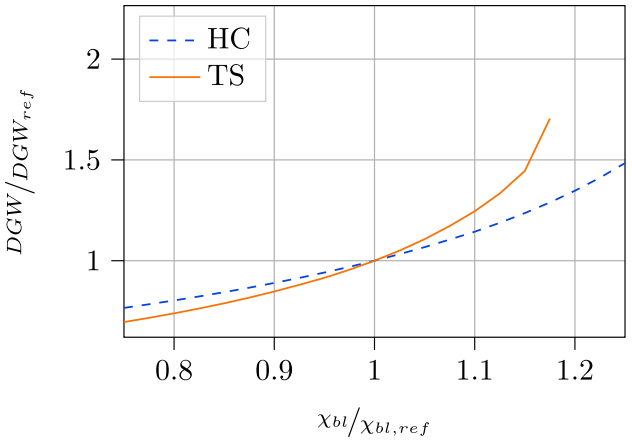

Fig. 19 Dependence of sized DGW from blade weight technology factor for coaxial helicopter (HC) and tailsitter (TS). $DGW_{\text{ref}} = 21.5\,\text{kg}$ (HC) $26.4\,\text{kg}$ (TS) $\chi_{\text{bl,ref}} = 1.0$ (HC) 1.0 (TS)

the results for the blade technology factor $K_{\text{tech,blade}}$. At the design point the tailsitter design shows a significantly higher sensitivity towards blade weight. An increase of 18 % leads to NDARC not finding a converged design solution which illustrates the importance of blade weight on the design and that the tailsitter design is generally more susceptible to such changes. For the wing weight this dependency is less pronounced.

The structural weight of the rotor blades is a main driving factor that causes the increase in DGW for most parameters investigated above. In this regard, it has to be noted that the weight models presented in Sect. 3.4 do not account for structural loads caused by higher aerodynamic loading, dynamic loads or requirements such as the mentioned flap eigenfrequency. In proximity to the respective design points at which the static structural safety factor is evaluated the models are assumed to be adequate. However, to conclusively examine these effects a more detailed design investigation is necessary. The tools NDARC, CAMRAD II, SONATA and VABS that were already used here could be more tightly coupled for such an investigation to iteratively examine structural loads and blade dynamics.

The contingency weight factor $f_{w,\text{cont}} = 20\,\%$ aims to consider uncertainties in the modeling. For the helicopter configuration, the published research regarding the MH serves as data basis so that 20 % is regarded as sufficient.

For the tailsitter, it is assumed that the same model assumptions also apply which is an additional source of uncertainty and could be taken into account through a higher contingency weight. Fig. 20 shows the influence of variations in $f_{w,\text{cont}}$ on the aircraft weight. The sensitivity is significantly higher for the tailsitter so that the sizing calculations diverge earlier and no value above $f_{w,\text{cont}} = 25\,\%$ leads

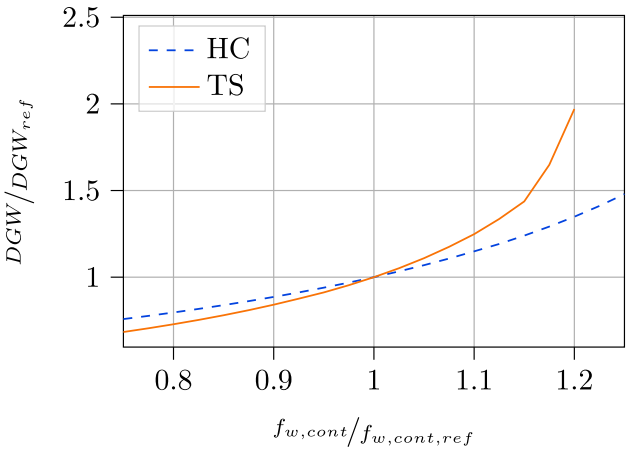

Fig. 20 Dependence of sized DGW from contingency weight factor for coaxial helicopter (HC) and tailsitter (TS). DGW_{ref} = 21.5 kg (HC) 26.4 kg (TS) $f_{w,\,\mathrm{cont,\,ref}}$ = 0.2 (HC) 0.2 (TS)

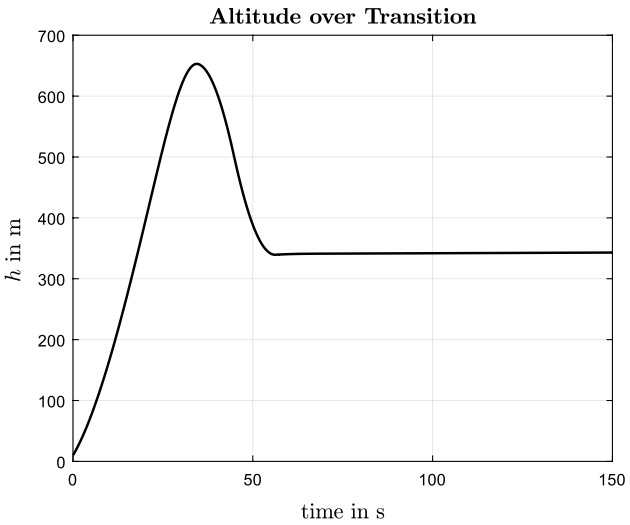

Fig. 21 Simulated flight altitude during transition maneuver of tailsitter

to a result. This dependency underlines the challenges that designing and building a transition configuration for Mars entails. Even small deviations from the expected weight estimations could lead to an unfeasible aircraft design. It also highlights that this configuration is much more sensitive to potential component weight increase and subsequently the design tolerates less weight penalty. Hence, the coaxial configuration is the more robust design choice in this regard.

4.3 Control characteristics

As mentioned in Sect. 1 the tailsitter configuration has to fly a climb and descent maneuver to transition from vertical take-off to level cruise flight. To evaluate the overall control characteristics and especially the feasibility of this maneuver a Desired Response model is developed [38]. This model can be used to evaluate whether a given configuration meets control requirements at any point in a mission. For this work it is used to derive the height of the trajectory needed to gain cruise speed during the transition of the tailsitter. Fig. 21 shows the simulated altitude during the transition for a cruise at an altitude of $h = 350$ m.

It shows that the tailsitter has to climb to a substantially higher altitude than the cruise altitude to gain sufficient speed during descent to reach cruise speed. The influence of the center of gravity position is investigated in regards to control authority during the transition. For this investigation, assumptions for the position of the components shown in Table 4, are made. It is found that if the center of gravity is located more than 2 cm forward of the neutral point, the control authority of the flaperons at the trailing edge of the wing becomes insufficient. The current position of $x_{CG} = 5$ cm does not fulfill this criterion. However, a more detailed design is necessary to conclusively evaluate the control authority of the tailsitter. For the helicopter configuration no control issues were identified.

5 Conclusions

In this presented study, two VTOL configurations were investigated in regards to their suitability as high range scout UAVs as part of the Valles Marines Explorer initiative. A coaxial helicopter based on the NASA Mars Helicopter Ingenuity and a transition tailsitter were modeled using the preliminary design software NDARC. To improve modeling accuracy of the rotor power and component weight, comprehensive analysis and 2D-FEM modeling were employed. The initial design mission was derived from VaMEx requirements, which is defined by a total range of 30 km and a payload capacity of 1.4 kg. The following conclusions can be drawn:

- A tailsitter designed for this range requires less energy and thereby battery weight than a helicopter sized for the same mission because of the superior cruise efficiency of the transition configuration. However, the added weight of wing and stabilizers leads to an overall higher design gross weight.
- For higher mission ranges above 30 km it was found that the DGW of aircrafts rises rapidly. Above 40 km the tailsitter shows a performance advantage to the helicopter. However, at this point the sized aircrafts are significantly heavier and larger than the baseline. Furthermore, this range is close to the convergence boundary at 45 km.

Therefore, the optimal range defined for the VaMEx mission of 100 km is considered to be unfeasible with either configuration.

- A sensitivity study of model parameters was conducted to investigate the influence of differing model assumptions. The design atmospheric density ρ was found to be a significant influence that requires additional input from a finalized mission definition and precise atmospheric data. The investigation of weight and performance model parameters highlights that the tailsitter design has higher sensitivities to component weight. Potential for possible improvements of the tailsitter configuration was found in the cruise speed v_{cruise} and the wing lift coefficient $C_{L,\text{ wing, des}}$.
- In addition to design sizings, an investigation of the control characteristics of both configurations was conducted. It showed that while the helicopter fulfills all handling requirements the tailsitter configuration is too stable due to its center of gravity position so that control authority of the trailing edge flaperons is not sufficient.
- Further challenges and uncertainties arise when considering a transition configuration, like the tailsitter, for deployment on Mars. The overall aircraft design complexity is higher because of the added wing and flaperons. Testing such an aircraft on Earth is more difficult, especially the transition maneuver is complicated to validate.

In conclusion, this study showed that designing a tailsitter aircraft for the presented mission requirements is significantly more challenging than a helicopter configuration. Considering, that a robust design approach is imperative to a successful VaMEx swarm exploration mission, the tailsitter configuration can therefore be deemed less suitable as a high range scout UAV than the helicopter configuration.

A successor project is planned that aims to study a rotor designed for Mars in detail. In these studies, a full-scale rotor will be tested in a simulated Martian atmosphere. The work is expected to produce valuable data for a successive final aircraft design and it aims to produce a first iteration prototype of the UAV rotor system.

Acknowledgements This work was funded by the German Space Agency at DLR through the VaMEx initiative with coordination by Dr. Oliver Funke and scientific consultation by Dr. Volker Klein. The authors thank Dominik Komp for support with CAMRAD II simulations and Jonas John for his contribution to the setup of the initial sizing methodology and framework. In addition the work of Maximilian Söpper and his colleagues at the institute of flight system dynamics at TUM regarding control characteristics is greatly appreciated. The authors gratefully acknowledge Witold Koning at NASA Ames research center for providing Mars Helicopter airfoil polars.

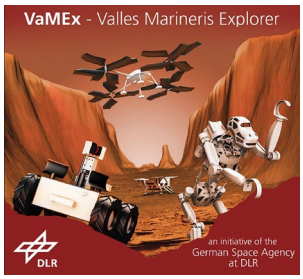

Funding Open Access funding enabled and organized by Projekt DEAL. Apart from the funding provided by the German Space Agency at DLR no additional funds, grants, or other support was received.

Declarations

Conflict of interest The authors have no competing interests to declare that are relevant to the content of this article.

References

1. Funke, O., Horneck, G.: The search for signatures of life and habitability on planets and moons of our solar system, pp. 457–481. Springer, Singapore (2018)
2. Committee on the Planetary Science and Astrobiology Decadal Survey, Space Studies Board, Division on Engineering and Physical Sciences & National Academies of Sciences, Engineering, and Medicine. Origins, Worlds, and Life: A Decadal Strategy for Planetary Science and Astrobiology 2023-2032 (National Academies Press, Washington, D.C., 2022)
3. NASA. Valles Marineris-NASA's Mars Exploration Program (2021). https://mars.nasa.gov/resources/3874/valles-marineris/. Accessed 30 Dec 2022
4. Reed, R.D.: High-flying mini-sniffer RPV - Mars bound? Astronaut. Aeronaut. **16**, 26–39 (1978)
5. Smith, S. C., Hahn, A. S., Johnson, W.: The Design of the Canyon Flyer, An Airplane for Mars Exploration. 38th Aerospace Sciences Meeting and Exhibit. (2000)
6. Braun, R., Wright, H., Croom, M., et al.: Design of the ARES Mars airplane and mission architecture. J. Spacecr. Rockets **43**(5), 1026–1034 (2006). https://doi.org/10.2514/1.17956
7. Anyoji, M., Nagai, H., Oyama, A.: Evaluation of aerodynamic performance of mars airplane in scientific balloon experiment. Fluid Mech. Res. Int. J. (2017). https://doi.org/10.15406/fmrij.2017.01.00012

8. Young, L., Aiken, E., Gulick, V.: Rotorcraft as mars scouts. IEEE Aerospace **1**, 1–378 (2002)
9. Balaram, B. et al.: Mars Helicopter Technology Demonstrator. 2018 AIAA Atmospheric Flight Mechanics Conference (2018)
10. NASA. Mars Helicopter - NASA Mars (2021). https://mars.nasa.gov/technology/helicopter/. Accessed 30 Dec 2022
11. Young, L., Aiken, E., Lee, P., Briggs, G.: Mars rotorcraft: Possibilities, Limitations, and Implications for human/robotic exploration. IEEE Aerospace, pp 300–318 (2005)
12. Young, L. A., Field, M., Aiken, E. et al.: The Future of Rotorcraft and other Aerial Vehicles for Mars Exploration. Vertical Flight Society 77th Annual Forum & Technology Display (2021)
13. Williams, D. R.: Mars Fact Sheet (2021). https://nssdc.gsfc.nasa.gov/planetary/factsheet/marsfact.html. Accessed 30 Dec 2022
14. Reiss, P.: Design of a UAV Concept for the Mars Valles Marineris Exploration. Master's thesis, Technical University Munich (2016)
15. Millour, E., Forget, F., Spiga, A. et al.: The Mars climate database (Version 5.3.). Scientific Workshop:"From Mars Express to ExoMars" (2018). http://www-mars.lmd.jussieu.fr. Accessed 30 Dec 2022
16. Forget, F., Hourdin, F., Fournier, R., et al.: Improved general circulation models of the Martian atmosphere from the surface to above 80 km. J. Geophys. Res. Planets **104**(E10), 24155–24175 (1999). https://doi.org/10.1029/1999JE001025
17. Johnson, W.: NDARC - NASA Design and Analysis of Rotorcraft Theoretical Basis and Architecture. AHS Aeromechanics Specialists, pp 778–803 (2010)
18. Meyn, L. A.: Rotorcraft optimization tools: Incorporating rotorcraft design codes into multi-disciplinary design, analysis, and optimization. AHS International Technical Meeting on Aeromechanics Design for Transformative Vertical Flight (2018)
19. Gray, J.S., Hwang, J.T., Martins, J.R.R.A., Moore, K.T., Naylor, B.A.: Openmdao: an open-source framework for multidisciplinary design, analysis, and optimization. Struct. Multidiscipl. Optim. **59**, 1075–1104 (2019). https://doi.org/10.1007/s00158-019-02211-z
20. Johnson, W.: NDARC - NASA Design and Analysis of Rotorcraft Validation and Demonstration. AHS Aeromechanics Specialists, 804–837 (2010)
21. Johnson, W.: NDARC 1.14 - Theory. Tech. Rep., NASA (2019). https://rotorcraft.arc.nasa.gov/Publications/files/NDARCTheory_v1_6_938.pdf. Accessed 30 Dec 2022
22. Pipenberg, B. T., Keennon, M. T., Langberg, S. A. Tyler, J. D.: Development of the Mars Helicopter Rotor System. Vertical Flight Society 75th Annual Forum and Technology Display, 1–10 (2019)
23. Koning, W.J.F., Johnson, W., Grip, H.F.: Improved Mars helicopter aerodynamic rotor model for comprehensive analyses. AIAA J. **57**(9), 3969–3979 (2019). https://doi.org/10.2514/1.J058045
24. McMasters, J.H., Henderson, M.L.: Low-speed single-element airfoil synthesis. Techn. Soaring **6**, 1–21 (1979)
25. John, J.: Preliminary Design Investigations of Rotorcraft-Configurations for the Exploration of Mars. Master's thesis, Technical University of Munich (2019)
26. Pflumm, T., Rex, W., Hajek, M.: A preprocessor for parametric composite rotor blade cross-sections. 44th European Rotorcraft Forum, pp 1223–1232 (2018)
27. Cesnik, C.E., Hodges, D.H.: VABS: a new concept for composite rotor blade cross-sectional modeling. J. Am. Helicopter Soc. **42**(1), 27–38 (1997). https://doi.org/10.4050/JAHS.42.27
28. Withrow, S., Johnson, W., Young, L. A. et al.: Mars Science Helicopter Conceptual Design. Tech. Rep., NASA (2020). https://ntrs.nasa.gov/search.jsp?R=20200002139. Accessed 30 Dec 2022
29. Fujioka, N., Nonomura, T., Oyama, A. et al.: Computational Analysis of Aerodynamic Performance of Mars Airplane. Transactions of the Japan Society for Aeronautical and Space Sciences, Aerospace Technology Japan **12** (ists29), Tk_1–Tk_5 (2014). https://doi.org/10.2322/tastj.12.tk_1
30. Rex, W., Pflumm, T. , Hajek, M.: Enhanced Efficiency And Flight Envelope by Variable Main Rotor Speed For Different Helicopter Configurations. 42nd European Rotorcraft Forum (2016)
31. Selig, M.: Summary of low speed airfoil data. SoarTech Publications (1995)
32. Traub, L.W., Coffman, C.: Efficient low-Reynolds-number airfoils. J. Aircr. **56**(5), 1987–2003 (2019). https://doi.org/10.2514/1.C035515
33. Winslow, J., Otsuka, H., Govindarajan, B., Chopra, I.: Basic understanding of airfoil characteristics at low Reynolds numbers (104–105). J. Aircr. **55**(3), 1050–1061 (2018). https://doi.org/10.2514/1.C034415
34. Hoerner, S.F.: Fluid-dynamic drag. Hoerner Fluid Dynamics (1965)
35. Blosiu, J., Bugga, R., Brandon, E. et al. Energy Storage Technologies for Future Planetary Science Missions Work Performed under the Planetary Science Program Support Task. Tech. Rep., NASA (2017). https://solarsystem.nasa.gov/resources/549/energy-storage-technologies-for-future-planetary-science-missions/. Accessed 30 Dec 2022
36. ROAMX. https://rotorcraft.arc.nasa.gov/Research/Programs/roamx.html. Accessed 30 Dec 2022
37. Koning, W.J., Romander, E.A., Johnson, W.: Optimization of Low Reynolds Number Airfoils for Martian Rotor Applications Using an Evolutionary Algorithm. American Institute of Aeronautics and Astronautics, Reston, Virginia (2020)
38. Zappek, V. et al.: Valles Marineris Explorer - Mars High Range Scout: Abschlussbericht VaMEx-MaHRS. Tech. Rep., Technische Universität München, Garching (2022). https://doi.org/10.2314/KXP:1810227674